Modelling the geometry of Coulomb thrust wedges

Genene Mulugeta

The Hans Ramberg Tectonic Laboratory, Box 555, S-751 22 Uppsala, Sweden

Abstract—Internal geometry and detachment of Coulomb thrust wedges is examined in a combined gravity and pressure force field under various boundary conditions and Coulomb parameters. Frontally buttressed sand wedges accreted with narrow tapers above soles with negligible friction. In these models, serial imbricates stepped-up in conjugate sets which operated synchronously or serially. With increases in sole friction, model Coulomb wedges accreted in piggyback style with enhanced taper but narrower spacing of imbricates. In this mode, flat-topped box-fold anticlines nucleated at the frontal tip of a sole thrust prior to the fore-limb failing as a ramp. The initial ramp-thrusts subsequently rotated and steepened to acquire concave-upwards listric geometry. When cohesion was a significant component of strength, and the sand grains interlocked thoroughly, ramp climb during piggyback thrusting occurred through the generation of a stack of backthrusts. The taper of cohesionless sand wedges, which lack any length scale, was consistent with the critical cohesionless Coulomb wedge taper. In contrast, the taper of experimental cohesive sand wedges, which are scale-dependent, was consistent with the theoretical cohesive Coulomb narrow taper, only when the cohesive length scale was $l_c \sim S_t/\varrho_t a_t \leq 10^{-6}$. This was constrained by comparing geometry of cohesive sand wedges shortened at different body force per unit mass.

INTRODUCTION

Davis *et al*. (1983) and Dahlen *et al*. (1984) considered the mechanics of fold–thrust belts and accretionary wedges (whose essential geometric characteristics have been outlined by Chapple 1978) as analogues to a wedge of snow or soil in front of a moving bulldozer. These authors presented an analytical theory which predicts the critical taper of compressional wedges applicable to common clastic sediments and rocks in the shallow brittle regime of the Earth's crust, which deform according to the empirical Coulomb failure criterion, modified to account for the weakening effects of pore fluid pressure. The critical taper is a function of wedge material strength and basal décollement response. Both nature and experiments confirm that strong basal detachments generate wedges with steep taper, whereas, incompetent glide horizons (e.g. salt) support broad wedges with narrow taper. At critical taper a Coulomb wedge is on the verge of shear failure throughout including the basal décollement (Davis *et al*. 1983). A subcritical wedge deforms internally to attain its critical taper, while a supercritical wedge slides stably when pushed. External factors such as erosion and isostatic subsidence promote internal deformation and drive a critical wedge into the subcritical domain (Davis *et al*. 1983, see also the erosion–accretion model of Mulugeta & Koyi 1987). Increase in sole friction may promote internal deformation and hence produce a steeper critical wedge. In contrast, sedimentation and decrease in sole friction may make a critical wedge supercritical.

In this paper the mechanics of Coulomb wedge accretion is studied by shortening isotropic cohesionless and/ or cohesive sands, under different body force per unit mass, above soles with different coefficients of sliding friction, and/or viscous resistance. The purpose is to examine the mechanics of accretion of model Coulomb wedges in the light of analytical theory that predicts the critical taper of Coulomb thrust wedges (Davis *et al*. 1983, Dahlen *et al*. 1984).

EXPERIMENTAL SET-UP AND PROCEDURE

The squeeze-box used to shorten specimens under normal gravity is illustrated in Fig. 1. The vertical moving platen is driven by an electric motor geared to provide a wide range in convergence rate $5 \times 10^{-3} - 5 \times 10^{-1}$ cm s^{-1}. A hydraulic squeeze-box driven by the centrifugal body force was used to shorten models in a centrifuge; the principles of this new technique are outlined in Mulugeta (1988). A magnetic valve connected to the hydraulic system, via an electrical slip ring assembly, controlled the onset and/or termination of lateral shortening. Using such a procedure it was possible to study the dynamics of thrust wedges at the scale of thrust–fold belts and/or accretionary wedges. In order to study the role of basal slope in detachment, the squeeze-box was placed on appropriately framed Plexiglass wedges so as to provide a sloping surface with respect to the equipotential surface of the centrifuge cups. In the models, fine internal structures were exposed by vacuum erosion (see Mulugeta & Koyi 1987 for the technical procedure) and/or by congelation (see Appendix).

COULOMB PARAMETERS AND SCALING

A fundamental premise of Coulomb theory (Brace & Kohlstedt 1980, Davis *et al*. 1983, Dahlen *et al*. 1984) and a rationale for the experimental investigations is that rock behaviour at upper crustal levels is controlled by

pressure-dependent, but rate-independent, Coulomb rheology

$$\tau = S + \sigma(1 - \lambda) \tan \phi, \qquad (1)$$

where τ is the shear strength, S is cohesion, ϕ is coefficient of internal friction, σ is normal stress, λ is the pore pressure ratio (Hubbert & Rubey 1959).

Coulomb behaviour is appropriately modelled using sand as a material analogue (Hubbert 1951, Davis *et al.* 1983), whose Coulomb strength and detachment response is shown in Fig. 2. Two types of sand have been used: (1) sand with bulk densities in the range 1.4 ± 0.1 g cm^{-3}, and grain sizes in the range (0.18–0.20 mm) containing mainly pure quartz sand; (2) sand with grain sizes in the range 0.08–0.18 mm and bulk densities in the range 1.2 ± 0.1 g cm^{-3} containing in addition to quartz, mica flakes, subangular feldspar, tourmaline, hematite, magnetite and rutile. In these materials, cohesion as well as coefficients of internal and detachment friction increased with compaction. The type 2 sand having more angular particles interlocked more thoroughly with compaction than the more rounded particles of type 1 sand. As a result, this material exhibited a greater increase in friction angle and cohesion with compaction than the type 1 sand (compare Figs. 2b & d). The increase in cohesion was a consequence of decrease in porosity. The type 2 sand suffered about 14% loss in volume with compaction, i.e. about twice as much as the type 1 sand for the same gravity load (~0.4 M Pa). The Mohr strength and failure envelopes (drawn by linear regression) are shown in Fig. 2. Cohesion of the compact sand materials varied by ±33%; this was constrained by linear regression on three to four repeated measurements during the same test. This produced similar order

of magnitude errors in scaling estimates. In the pre-compacted sand materials subsequently shortened under normal gravity, cohesion was a significant component of strength. However, in the tests shortened in a centrifuge this small cohesion was of no consequence.

This may be understood from the dynamical similitude of Coulomb materials deforming at different body force per unit mass. To maintain similarity the non-dimensional ratio between the cohesive strength S, and the product of the density ϱ, length scale l and acceleration a must be invariant between models deforming at different body force per unit mass:

$$\frac{S}{\varrho a l} = k. \qquad (2)$$

Equation (2) would be accurate if dynamic scaling is governed by the cohesive strength of the Coulomb materials. Thus, for otherwise similar models, deforming at different body force unit mass, e.g. under normal gravity (g) and in a centrifuge (a):

$$\frac{S_g}{\varrho g l} = \frac{S_c}{\varrho a l}, \qquad (3)$$

where S_g is cohesive strength under normal gravity and S_c is cohesive strength in a centrifuge. Thus, from the above analysis, to maintain similarity, g/a times weaker model materials must be used in tests shortened under normal gravity than corresponding centrifuge tests. Thus, compact type 2 sand with an average cohesion of ~176 Pa deforming in a centrifuge at 800g would behave in a similar manner as nearly cohesionless sand deforming under normal gravity. This would be true as long as cohesion is much smaller than the component of strength due to wedge internal friction in the Coulomb equation.
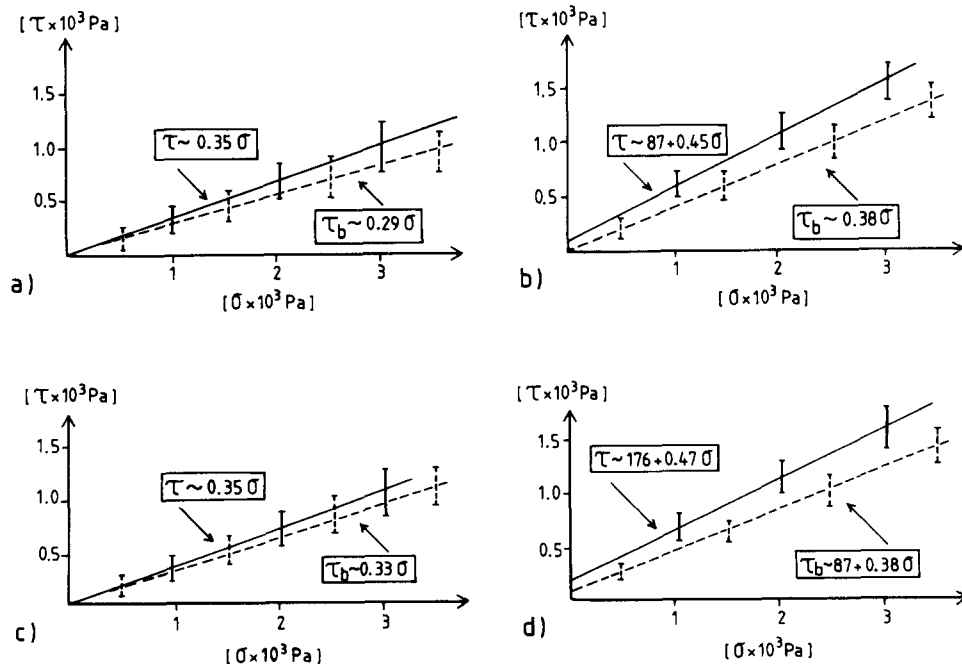

Fig. 2. Coulomb wedge strength (τ) and décollement response on Plexiglass (τ_b) of the sand materials used in the tests. (a) Loose type 1 sand, (b) compact type 1 sand, (c) loose type 2 sand and (d) compact type 2 sand. Detachment response of these materials on mercury was nearly frictionless.
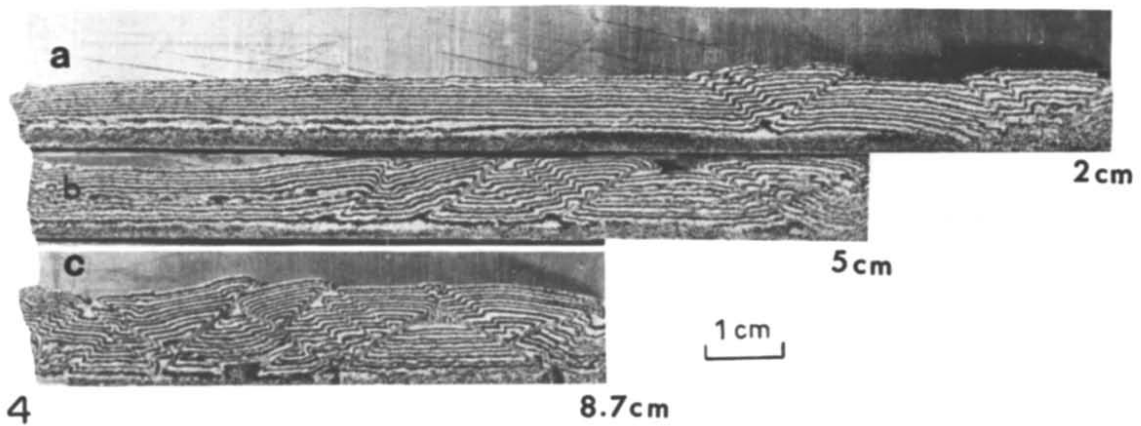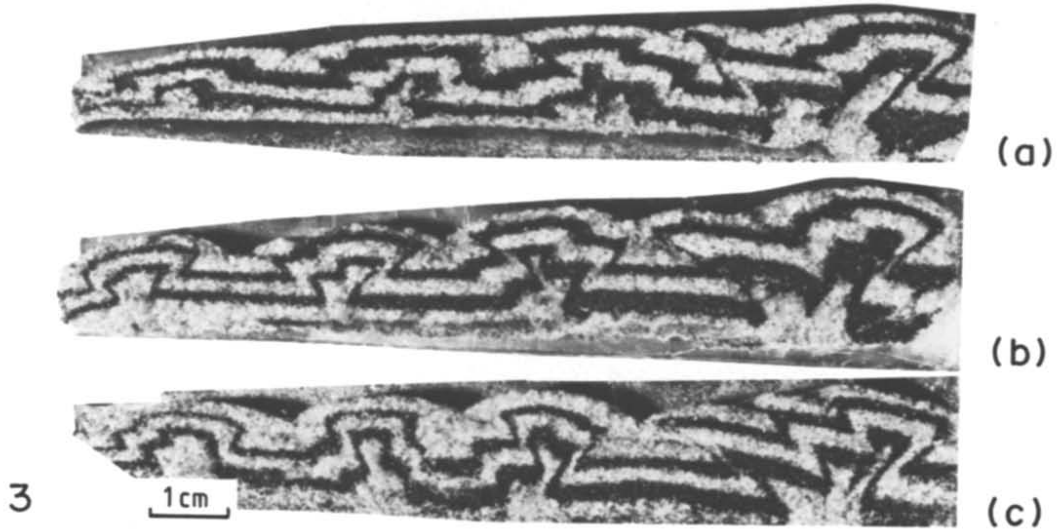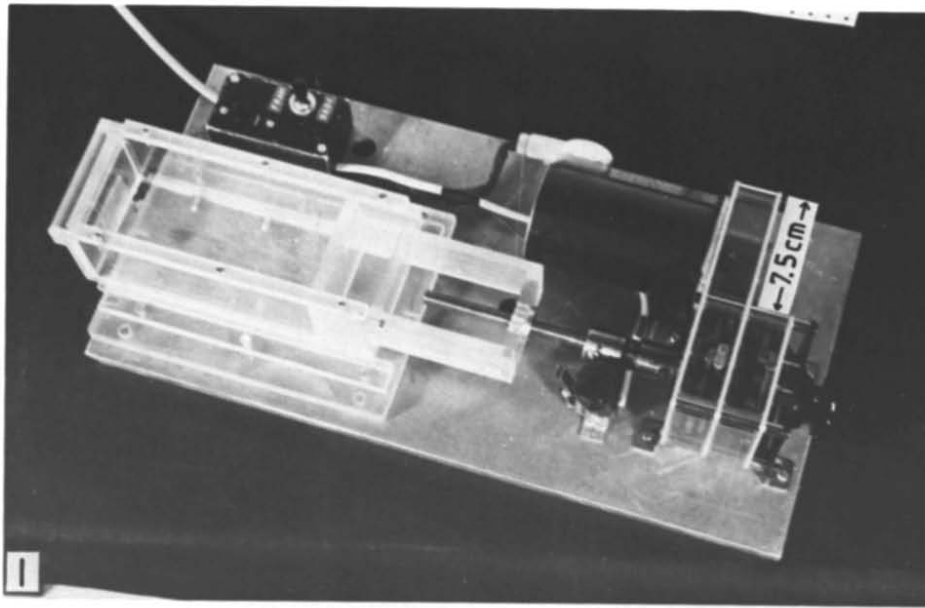
(a)

(b)

3

1cm

(c)

a

2cm

b

5cm

c

1cm

4

8.7cm

Fig. 1. Motorized squeeze-box used to shorten tests under normal gravity.

Fig. 3. (a)–(c) Different cross-sections of thrust wedges of loose type 1 sand shortened 7 cm above mercury.

Fig. 4. Loose type 2 sand shortened under normal gravity and accreting above mercury. Numbers in Figs. 4–9 indicate shortening displacements.
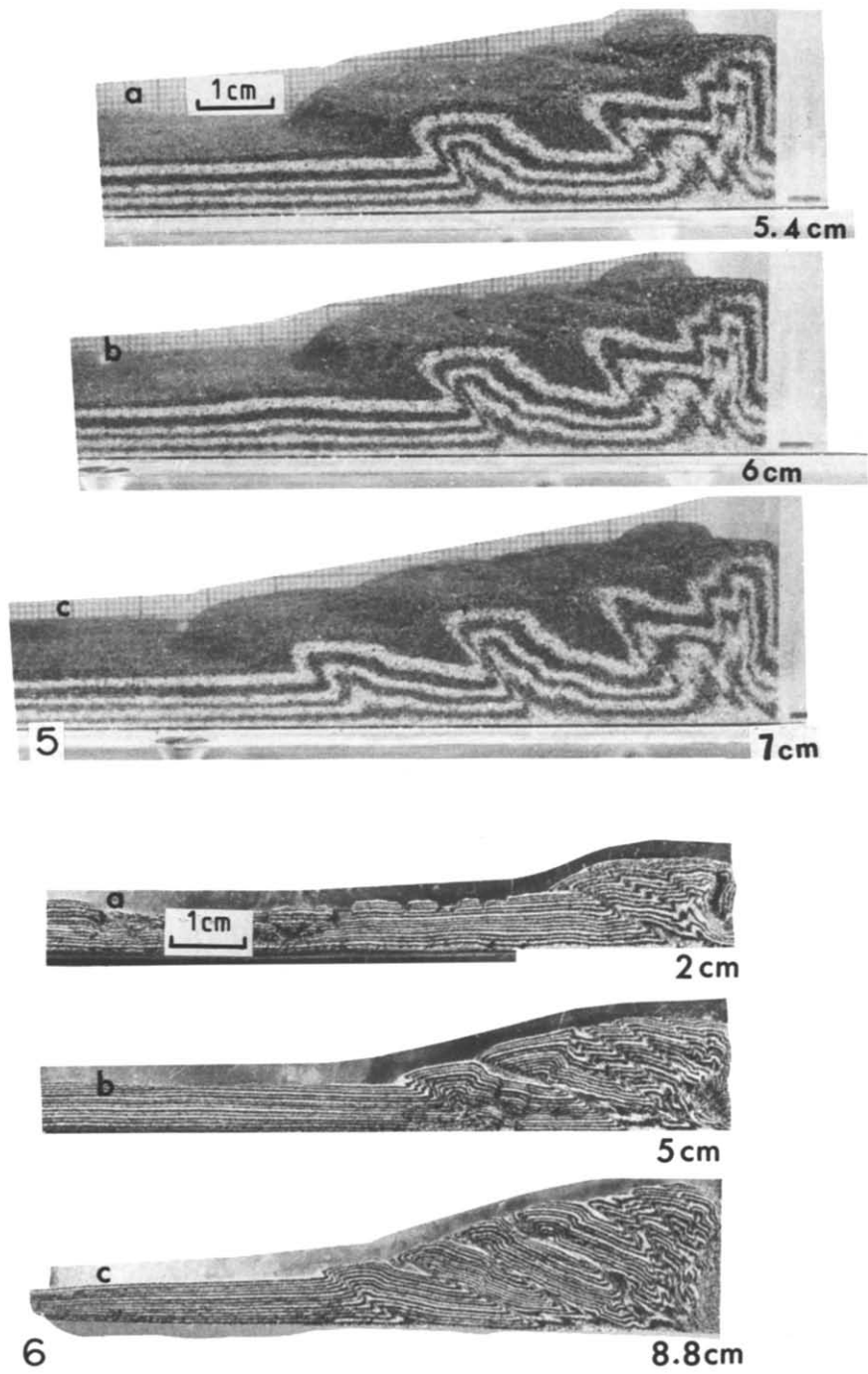
Fig. 5. Loose type 1 sand shortened under normal gravity and accreting above Plexiglass. Initial length/thickness ratios in Figs. 5–8, varied in the range 20–26. Here only rear parts are shown to save space.

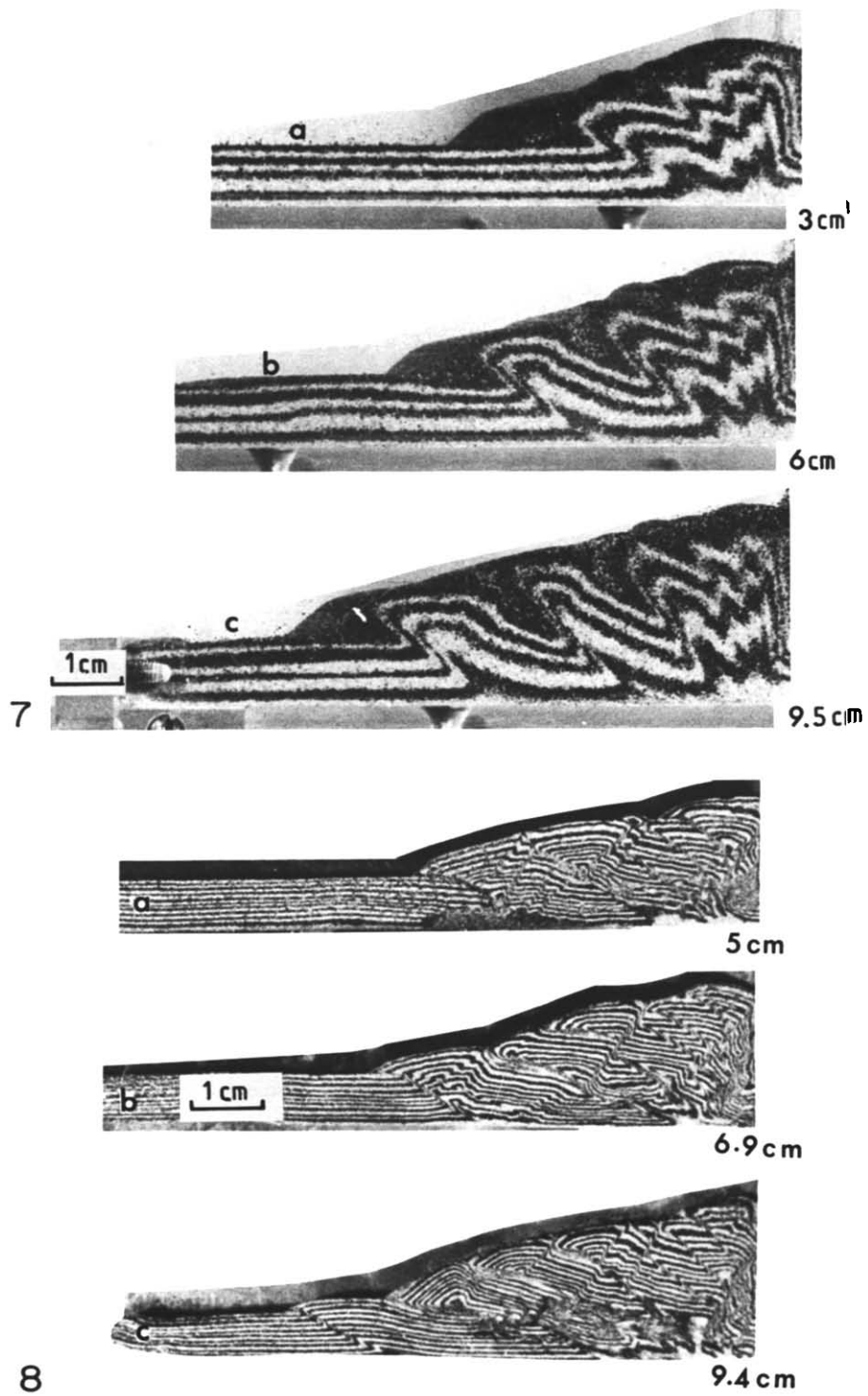Fig. 6. Same as in Fig. 5 using loose type 2 sand.

Fig. 7. Same as in Fig. 5 using compact type 1 sand.

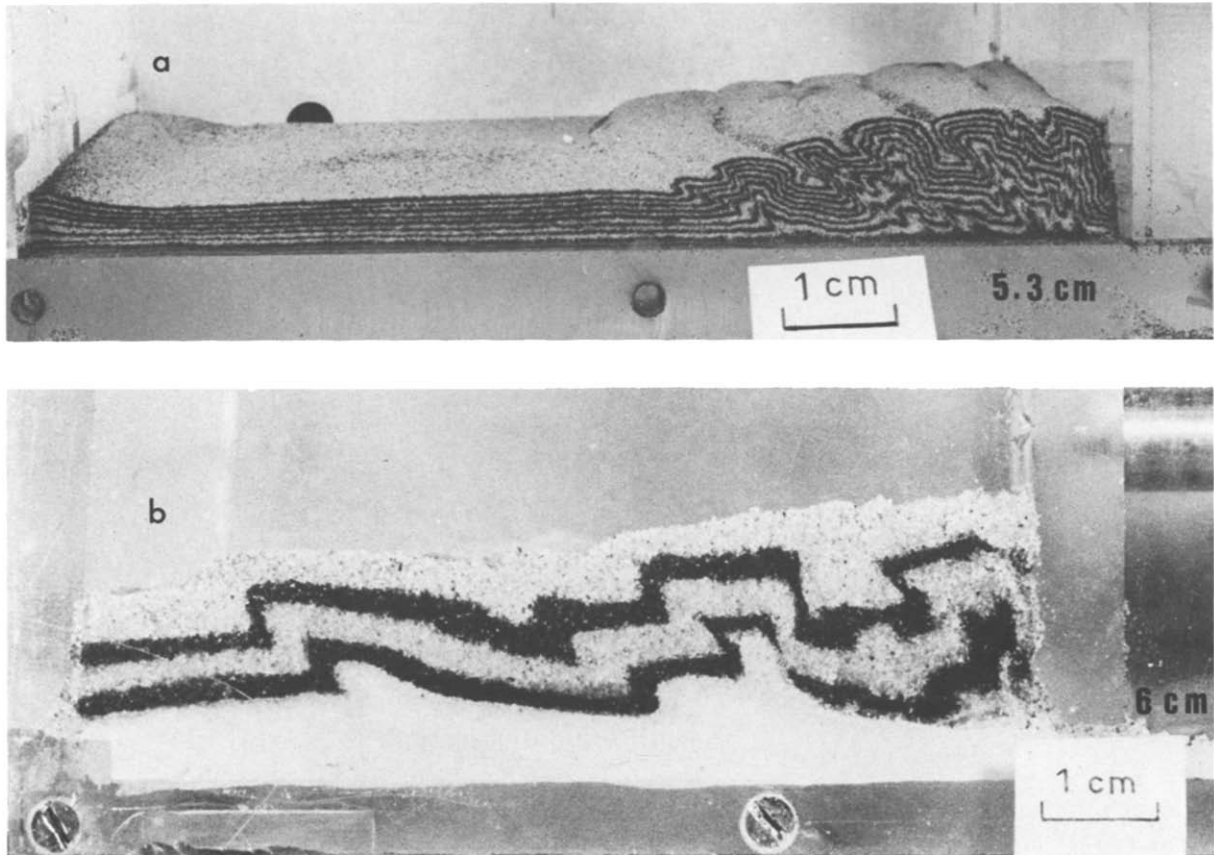Fig. 8. Same as in Fig. 5 using compact type 2 sand.

Fig. 9. Thrust wedges shortened in a centrifuge and detached on Plexiglass. (a) Compact type 2 sand. (b) Damp cohesive type 1 sand riding above a viscous substratum ($\mu \approx 3 \times 10^4$ Pa s, $\varrho \sim 1.1$ g cm^{-3}).

The same reasoning can also be applied to natural sedimentary rocks which exhibit low-cohesion of 5–20 M Pa (e.g. Hoshino *et al*. 1972). At depths of a few km, the effect of such a low cohesion is unimportant in comparison with the pressure-dependent term in the Coulomb equation. Such an analysis is important in understanding the role of cohesion in wedge taper.

GEOMETRY OF SEQUENTIAL ACCRETION

In models shortened above low-friction detachments, imbricate thrusts stepped up in conjugate sets which operated synchronously (Figs. 3a–c), or serially (Figs. 4a–c). The imbricates show convex-upwards geometry in cross-section. In the serially operating conjugate imbricates, climb on initial backthrust ramps generated forward-directed imbricate stacks (Figs. 4a–c). The backthrusts nucleated serially in a forward sequence with steepening geometry and locked at moderate dip angles (Fig. 4c). These were subsequently disrupted by forward-verging imbricates. The symmetrical imbricates and box-fold anticlines which developed above low-friction/low-viscosity detachments (Figs. 3, 4 and 9b) correlate well with similar structures above weak frictional and/or viscous detachments (e.g. salt, gypsiferous beds, and marls in the Jura, Appalachians, etc., Laubscher 1977, Chapple 1978).

With increase in sole friction, model sand wedges accreted in piggyback style (Figs. 5–9a). At higher stages of bulk shortening, box-fold anticlines nucleated at the distal tip of a sole thrust prior to the forelimb failing as a ramp. During accretion, slump detritus of type 1 sand derived from the top layers of ramp anticlines was incorporated into the footwalls (Figs. 5a–c and 7a–c). This is rather similar to erosional detritus which accumulates in front of actively moving natural thrust sheets and which subsequently gets overridden by the thrust sheet (Elliott 1976). During sequential accretion the imbricate sheets rotated and steepened in response to the forward migration of the zone of active shortening with time. A compacted equivalent of the type 1 sand accreted with even higher taper but with nearly similar internal structures when subsequently shortened under normal gravity. This was due to enhancement of sole friction associated with the compacting process (Figs. 7a–c).

The pre-compacted cohesive type 2 sand also accreted with a high taper when subsequently shortened under

normal gravity (Fig. 8). In this model, piggyback thrust sheets were unstable and deformed by back thrusting during ramp climb. These subsequently formed a linked pattern transecting the piggyback wedge (Figs. 8a–c). Compact type 2 sand shortened at different body force per unit mass (cf. Figs. 8 and 9a) shows the importance of cohesion in the mechanics of back thrusting. For example, when cohesion was a significant component of strength, climb along forethrust ramps took place by generating a stack of backthrusts (Fig. 8), whereas, when the same material was shortened in a centrifuge at 800*g* (apparently deforming as cohesionless sand) backthrusts were nearly absent (Fig. 9a). The piggyback mode of thrust propagation is well documented in thrust–fold belts (e.g. Boyer & Elliott 1982). Figure 9(b) shows a narrow cross-sectional taper of a Coulomb wedge riding above a viscous substratum. Such a model mimicks the bulk geometry of clastic wedges shortened and detached above salt (e.g. Davis & Engelder 1985). The greater stacking of thrust sheets towards the rear would load the ductile substratum thereby generating a greater degree of isostatic adjustment (Fig. 9b).

COMPARISON WITH CRITICAL WEDGE TAPER ANALYSIS

Davis *et al*. (1983) and Dahlen *et al*. (1984) presented steady state accretion of isotropic, time-independent, Coulomb wedges as analogues of fold–thrust belts. These models, though simple, proved successful in predicting the gross geometry of fold–thrust belts and accretionary wedges. An approximate form of the critical taper equation for dry cohesionless Coulomb wedges, may be derived from equations of static equilibrium (Fig. 10):

$$\frac{\partial \sigma_{xx}}{\partial x} + \frac{\partial \tau_{xz}}{\partial z} + \varrho g \sin \beta = 0 \qquad (4a)$$

$$\frac{\partial \tau_{xz}}{\partial x} + \frac{\partial \sigma_{zz}}{\partial z} - \varrho g \cos \beta = 0. \qquad (4b)$$

Neglecting the shear stress gradient in the transport direction $\partial \tau_{xz}/\partial x$ which is likely to be small compared with the vertical gradient in normal stress $\partial \sigma_{zz}/\partial z$, equation (4b) reduces to:

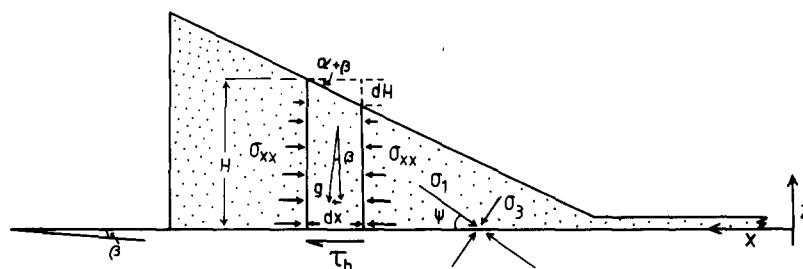$$\frac{\partial \sigma_{zz}}{\partial z} = \varrho g \cos \beta. \qquad (5)$$

Fig. 10. Force balance in a critically tapered wedge.

Integrating equation (5) with respect to z gives:

$$\sigma_{zz} = \varrho g(H - z) \cos \beta. \tag{6}$$

If we assume that the wedge is on the verge of internal failure throughout, the failure criterion for a non-cohesive Coulomb wedge $\tau = \mu\sigma_n = \tan \phi\sigma_{zz}$ is satisfied along two planes oriented at angles $\pm\pi/4 - \phi/2$, at every point within the wedge. Denoting the local angle between the axis of maximum compression and the x-axis by ψ (Fig. 10), the state of stress within a cohesionless critical dry coulomb wedge may be expressed in terms of ψ, assuming a constant wedge internal friction angle (ϕ) (Davis *et al*. 1983):

$$\tfrac{1}{2}(\sigma_{xx} - \sigma_{zz}) = \frac{\sigma_{zz}}{\csc \phi \sec 2\psi - 1} \tag{7}$$

$$\tau_{xz} = \tan 2\psi \frac{\sigma_{zz}}{\csc \phi \sec 2\psi - 1}. \tag{8}$$

Re-arranging equation (7):

$$\sigma_{xx} = \frac{2\sigma_{zz}}{\csc \phi \sec 2\psi - 1} + \sigma_{zz} = \sigma_{zz}(1 + k) \tag{9a}$$

$$k = \frac{2}{\csc \phi \sec 2\psi - 1}. \tag{9b}$$

Equation (9a) is the sum of the lithostatic load and the push term represented by k and substituting equation (9a) in (4a) gives:

$$\frac{\partial}{\partial x}[\sigma_{zz}(1 + k)] + \frac{\partial\tau_{zx}}{\partial z} + \varrho g \sin \beta = 0 \tag{10}$$

$$\frac{\partial}{\partial x}[\varrho g(H - z) \cos \beta(1 + k)] + \frac{\partial\tau_{zx}}{\partial z} + \varrho g \sin \beta = 0. \tag{11}$$

Integrating with respect to z, and at the base:

$$\frac{\partial}{\partial x}[-\tfrac{1}{2}\varrho gH^2 \cos \beta(1 + k)] + \tau_b + \varrho gH \sin \beta = 0. \tag{12}$$

For a constant surface slope ($dH/dx = \tan (\alpha + \beta)$, Fig. 10)

$$-\varrho gH \tan (\alpha + \beta) \cos \beta(1 + k) + \tau_b + \varrho gH \sin \beta = 0. \tag{13}$$

Using small angle approximations ($\cos \beta \sim 1$, $\sin \beta \sim \beta$, $\tan (\alpha + \beta) \sim (\alpha + \beta)$ gives:

$$-\varrho gH(\alpha + \beta)(1 + k) + \tau_b + \varrho gH\beta = 0. \tag{14}$$

Amonton's law assuming non-cohesive frictional law at the base gives

$$\tau_b = \mu_b\sigma_n = \mu_b\sigma_{zz} = \mu_b\varrho gH \cos \beta = \mu_b\varrho gH. \tag{15}$$

Substituting τ_b, from equations (15), in equation (14) gives:

$$-\varrho gH(\alpha + \beta)(1 + k) + \mu_b\varrho gH + \varrho gH \sin \beta = 0 \tag{16}$$

$$\alpha + \beta = \frac{\mu_b + \beta}{1 + k}. \tag{17}$$

The form of equation (17) is similar to the critical Coulomb wedge taper analysis of Davis *et al*. (1983) except for the important difference that here ψ is strictly constant; whereas in their equation k is a dimensionless quantity which varies with depth z

$$k = 2H^{-1} \int_0^H \frac{dz}{\csc \phi \sec 2\psi(z) - 1}.$$

An approximate expression for k, valid in the interval $0 < z < H$ (Davis *et al*. 1983) is

$$k \sim \frac{\sin \phi}{1 - \sin \phi} + \frac{\sin^2 \phi_b + \cos \phi_b(\sin^2 \phi - \sin^2 \phi_b)^{1/2}}{\cos^2 \phi_b - \cos \phi_b(\sin^2 \phi - \sin^2 \phi_b)^{1/2}}. \tag{18}$$

Moreover, in the case $\psi = 0$, principal stresses are approximately parallel to x and z, thus the critical taper equation (17) reduces to:

$$\alpha + \beta = (\mu_b + \beta)\left(\frac{1 - \sin \phi}{1 + \sin \phi}\right). \tag{19}$$

This result can also be derived using a value for $k = 2 \sin \phi/1 - \sin \phi$, in the critical taper equation of Davis *et al*. (1983) valid when the coefficient of sliding friction is much smaller than the coefficient of internal friction.

A complete form of the critical taper equation for cohesionless Coulomb wedges applicable also for submarine wedges has a form (Davis *et al*. 1983):

$$\alpha + \beta = \frac{(1 - \varrho_w/\varrho)\beta + (1 - \lambda_b)\mu_b}{(1 - \varrho_w/\varrho) + (1 - \lambda)k}, \tag{20}$$

where ϱ_w, ϱ are densities of sea water and wedge, respectively, λ, λ_b denote generalized pore fluid pressure ratios within the wedge and along the base, respectively. All other quantities are described above.

Comparison of the taper of model cohesionless sand wedges using the approximate k value used here, with the approximate k value of Davis *et al*. (1983) shows almost similar results, despite slight differences in k value <0.2 (Fig. 11). However, taper of loose type 2 sand wedges differed markedly (by 5–7°) as compared with the theoretical cohesionless taper equation (17). A possible explanation for this difference in taper may be the changing material response during accretion. Whereas, the theoretical taper equation assumes that density and the various Coulomb parameters, remain constant during accretion, the loose type 2 sand material compacted with accretion. Moreover, the model Coulomb wedges were not steady state features as suggested by the critical wedge taper analysis. Rather, they changed taper by 3–5° during sequential accretion (e.g. Figs. 5 and 6), suggesting that they deformed internally, while sliding stably, in order to incorporate new material at the toe. The laterally compacting sand wedges developed a convex cross-sectional profile in response to loss of volume during accretion. This geometry is well developed in type 2 loose sand which experiences a greater loss in porosity than the type 1 loose sand. This has a direct analogy with the convex
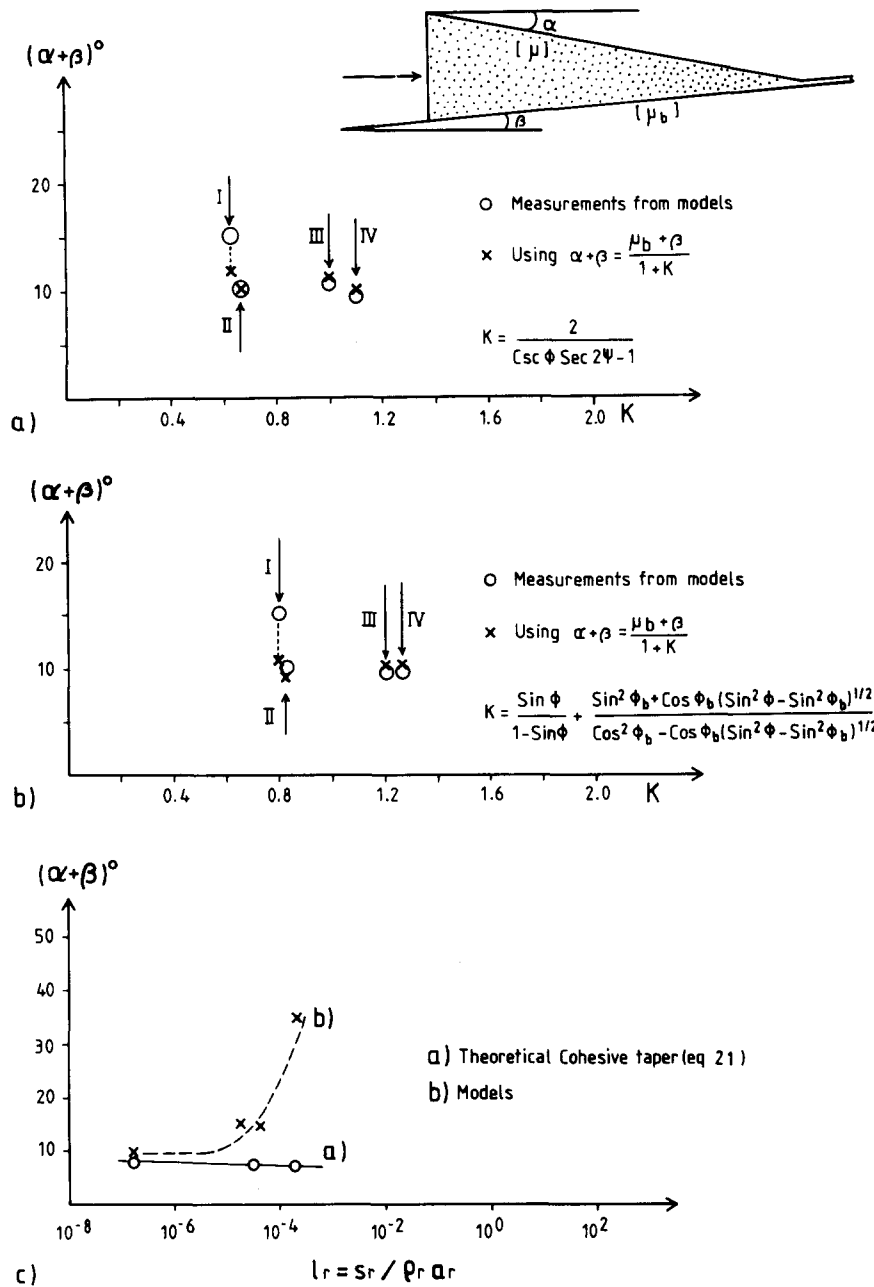
Fig. 11. Comparison of taper of model sand wedges deforming at different body force/unit mass and accreting above frictional décollement with the theoretical Coulomb wedge taper equation (17). Using k values of this paper, (b) using k values of Davis *et al.* (1983). I, II, III and IV, denote models shown in Figs. 6, 5 (not illustrated) and 9(a), respectively. Dots in I, denote the big gap between experiments and theory. (c) Comparison of theoretical cohesive wedge taper equation (21), with model cohesive taper, as a function of length scale.

geometry of laterally compacting accretionary wedges (Zhao *et al.* 1986).

The taper of cohesive sand wedges is strongly scale-dependent. For example, the model cohesive sand wedges which deform at a length scale: $l_r = S_r/\varrho_r a_r \sim 10^{-4}$ (where S_r, ϱ_r and a_r, denote model ratios of cohesive strength, density and body force per unit mass, respectively) show much steeper taper than in the theoretical Coulomb cohesive wedges equation (21) from Dahlen *et al.* (1984). In estimating the above length scale, a prototype cohesive strength of clastic sediments of 5 M Pa (Hoshino *et al.* 1972) and density of $\sim$2.4 g cm^{-3} were used.

$$\alpha + \beta = \frac{(1 - \varrho_w/\varrho)\beta + (1 - \lambda_b)\mu_b - Q(S/gr)\cot\phi}{(1 - \varrho_w/\varrho) + (1 - \lambda)k}.$$

(21)

where S is cohesion and r denotes radial distance from the origin at the toe. All other quantities are defined above and:

$$K = 4(\alpha + \beta)^{-2} \int_0^{\alpha+\beta} \frac{\theta \, d\theta}{\cosec \phi \sec 2\psi - 1}$$

$$Q = 2(\alpha + \beta)^{-1} \int_0^{\alpha+\beta} \frac{d\theta}{\cosec \phi \sec 2\psi - 1}.$$

In the above computations k, Q values at the base of wedge were used. Because of the scale-dependency, the taper of cohesive sand wedges (e.g. Figs. 7 and 8) was not in good agreement with the theoretical cohesive narrow taper (Dahlen et al. 1984). However, when the cohesive length scale was enhanced by two orders of magnitude or ($l_r \sim S_r/\varrho_r a_r \leq 10^{-6}$) by shortening in a centrifuge, the taper of model sand wedges was in much better agreement with the theoretical estimates of Dahlen et al. (1984) (Fig. 10c). Moreover, as cohesion was much smaller than the component of strength due to wedge internal friction ($S \ll \mu \varrho g H$), the critical taper equation for cohesive wedges approached the limiting taper corresponding to negligible cohesion. As a result, the taper of slightly cohesive sand wedges shortened in a centrifuge (e.g. Fig. 10a) and others not illustrated here were also consistent with the theoretical cohesionless Coulomb wedge taper (Davis et al. 1983).

SPACINGS OF IMBRICATE THRUSTS AND DÉCOLLEMENT FOLDS

The spacing of experimental décollement folds and imbricate thrusts was found to depend on initial length/thickness ratios above the basal décollement, material properties and coefficients of sliding friction, but not

convergence rate, which varied over three orders of magnitude. Low-friction detachments produced thinner wedges with wider spacing of imbricates (Figs. 3 and 4). The taper of thrust wedges increased and spacing of imbricates decreased with increasing friction along the sole (c.f. Figs. 5–9a), as is thought to be the case in natural thrust fold belts and accretionary wedges (Chapple 1978, Davis & Engelder 1985).

The average spacing/thickness ratio of serially nucleating imbricates/box-folds in both types of loose sand accreting on Plexiglass was ~4.8. This suggests that if cohesionless clastic sediments in nature deform according to the Coulomb criterion, and décollement strength is about ~20% lower than the strength of sediments, spacing/thickness ratios of imbricates/box-folds should be about 4.8 (Fig. 12a). Initial spacings between serial imbricates, which propagated in piggyback style were small and increased with progressive build-up of the thrust wedge. The rate of nucleation of imbricates was relatively fast until the thrust wedges attained their critical taper, and decreased after attainment of the critical taper (Figs. 12a & b). However, in natural settings such a systematically increasing sequencing of ramp spacing above an even and smooth décollement may be perturbed by: (1) pre-existing basement features; (2) erosion–deposition cycles; (3) facies changes in the sedimentary layering; and (4) variations in décollement parameters.
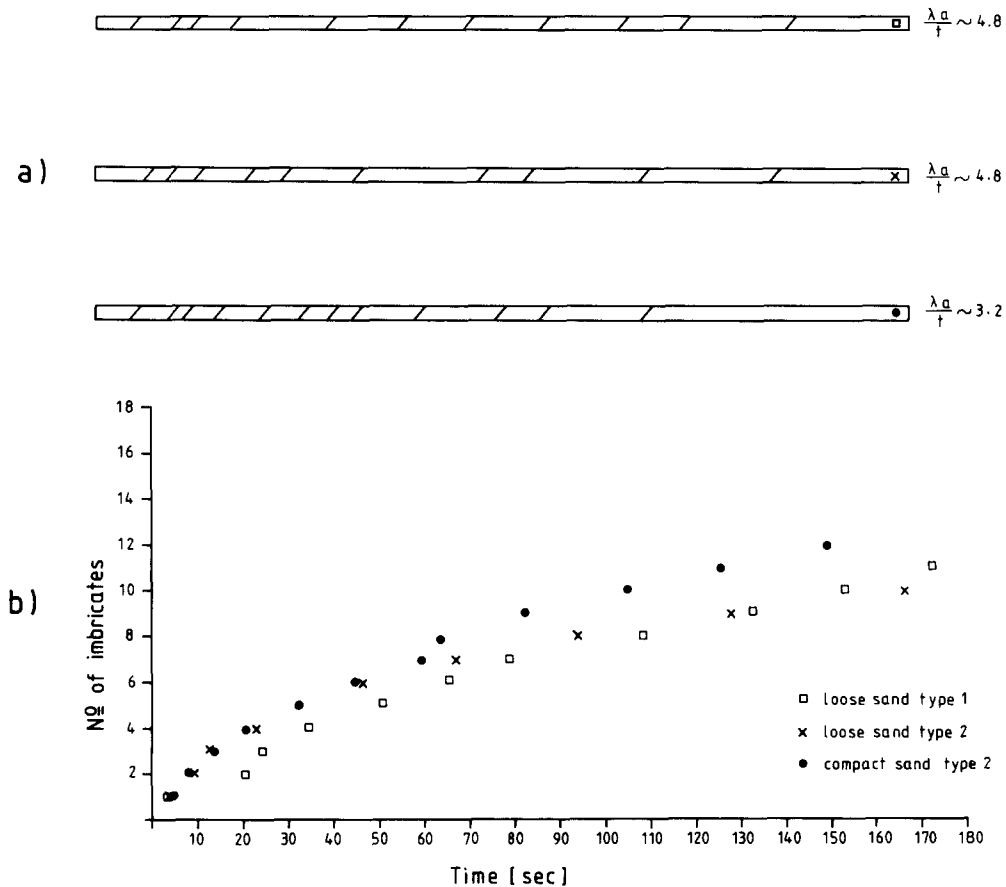

Fig. 12. (a) Initial spacings between serially nucleating imbricates in sand wedges with similar initial length/thickness ratio accreting above Plexiglass (see b for definition of symbols). (b) Nucleation rate of the same serial imbricates.

STEP-UP ANGLES OF IMBRICATES

Both theory and experiment confirm that forward-verging imbricates dip more shallowly with increase in the ratio of décollement strength to wedge strength (Figs. 13a–c). For example, essentially symmetrical imbricates, with nearly equal amounts of forethrusts and backthrusts, developed above low-friction detachments (c.f. Figs. 3 and 4). With increase in the ratio of décollement to wedge strength, the shallowly dipping forward thrusts predominated over backthrusts (Figs. 5–9).

Theoretically, the angle (ψ_b), at which the axis of maximum compression dips with respect to the sole, controls the orientation of Coulomb failure planes. This can be measured directly from the Mohr–Coulomb diagrams (e.g. Figs. 2a–d) or computed using equation (24) of Davis et al. (1983) for cohesionless wedges and the iterative solution, equation (29) of Dahlen et al. (1984), for cohesive wedges. The failure planes (θ) have equal

dips, oriented symmetrically about the (σ_1) axis (Hafner 1951). Forward-verging step-up angles are determined by $\delta_f = 45 - \phi/2 - \psi_b$, whereas, backthrusts step-up at an angle determined by $\delta_b = 45 - \phi/2 + \psi_b$ (Davis & Engelder 1985). However, the orientation of the measured failure plane of forward-verging imbricates in the models differed by ~10–20° (Fig. 13a), as compared to the potential failure planes that are expected theoretically from the Mohr–Coulomb criterion (Figs. 13c & d). The reasons for this discrepancy must be addressed. The macroscopic mode of compression in the models was not only accommodated by movement along localized shear faults but also involved layer shortening and ramp folding, achieved by gliding at the grain size scale. For example, imbrication in the type 1 sand material (at least at later stages of bulk shortening >10%) was by shearing along forelimbs of anticlines rather than as imbricates coinciding with the slip lines in a Coulomb material. This suggests that care should be taken in inferring wedge
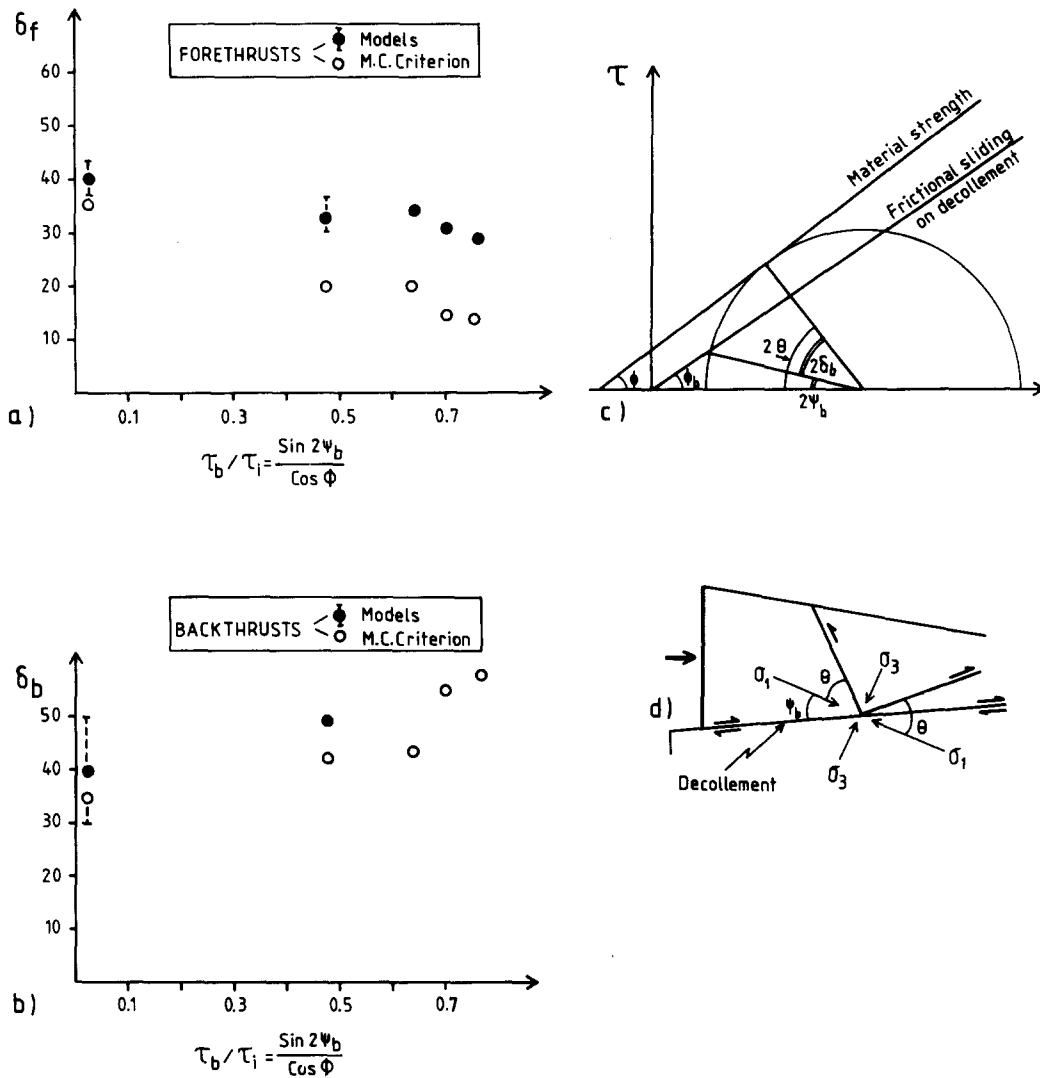

Fig. 13. Comparison of model step-up angles (solid circles) of (a) forethrusts (δ_f) and (b) backthrusts (δ_b) with theoretical step-up angles, based on the Mohr–Coulomb criterion (open circles), as a function of décollement to wedge strength ratios, bars indicate variations. (c) Mohr–Coulomb diagram illustrating graphically the relationships between the stress orientation angle ψ and the strength of the wedge and the basal décollement (after Davis & Engelder 1985). (d) Diagram showing why, in the presence of significant décollement strength, forward vergent planes dip more shallowly, because ψ is positive, than the backward-vergent planes (after Davis & Engelder 1985).

strength and décollement friction parameters based only on step-up angles of imbricates. Moreover, the models exhibited few faults, instead of the continuous state of failure within a theoretical critical Coulomb wedge (Davis *et al.* 1983, Dahlen *et al.* 1984).

RELATIVE SIGNIFICANCE OF A PUSH FROM THE REAR VERSUS GRAVITY IN OVERCOMING DÉCOLLEMENT RESISTANCE

The shear resistance that must be overcome in order to induce décollement can be computed from equation (14) which after re-arrangement of terms gives:

$$\tau_b = \varrho g H \alpha \left[1 + k \left(1 + \frac{\beta}{\alpha} \right) \right]. \tag{22}$$

Equation (22) is the relation between resistive and driving forces. The first driving term on the right-hand side is that due to gravity and the second term to the push from the rear. Davis *et al.* (1983) suggest that the contribution from the push from the rear in driving critically tapered compressive wedge is 4–5 times that due to gravity.

In this respect it is also interesting to estimate the relative significance of the push versus gravity force in emplacing the model thrust wedges. In systems with strict dynamic similarity, the ratio between forces in model and prototype should be constant when compared kind for kind. The ratio between gravity force/lateral force (x) or suggested Smoluchowski number (Ramberg 1981, p. 41) should be similar in dynamically similar systems.

$$\frac{F_g}{F_p} = x. \tag{23}$$

However, in some of the models (e.g. Fig. 9a) the ratio between pressure force/gravity force was about one order of magnitude greater than a corresponding natural thrust wedge. For example, whereas a push pressure of ~0.4 M Pa was sufficient to emplace the thrust wedge shown in Fig. 9(a), a push pressure of ~2 M Pa was employed in the actual shortening of the wedge (Fig. 14). Possible contributory factors which helped drive-up the emplacement pressure may be apparatus and sidewall friction.
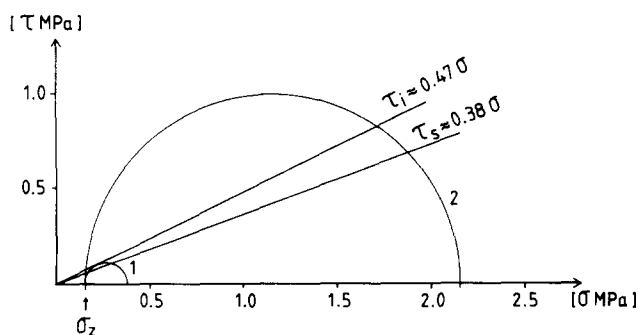

Fig. 14. Mohr circle representation of estimates of push pressure used in driving the model shown in Fig. 9(a), (1) shows push pressure necessary for accretion, (2) shows the push pressure employed in actual shortening of the wedge.

CONCLUSIONS

From model studies of the mechanics of Coulomb thrust wedges the following conclusions seem warranted:

(1) Low-friction detachments produced thinner wedges which required wider spacing of structures (box-folds, imbricates).

(2) In the piggyback mode of thrust propagation, spacings between serial imbricates increased with progressive wedge accretion.

(3) Linked listric back thrusts confined to a piggyback stack of imbricate sheets developed in materials with a high degree of cohesion and internal friction. In nature such structures are likely to develop in sediments which had undergone a higher degree of compaction prior to shortening.

(4) The model compressional wedges do not exhibit steady state taper with accretion. Also, laterally compacting sand wedges exhibited a convex cross-sectional profile as compared to the ideal triangular shape of a theoretical cohesionless Coulomb wedge.

(5) The fact that the macroscopic mode of compression in the models also involved layer shortening and ramp folding suggests that critically tapered model sand wedges may not be on the verge of localized shear failure throughout (unless sliding at the grain size scale is considered as a type of shear failure) as suggested by the critical Coulomb wedge taper analysis.

REFERENCES

Boyer, S. & Elliott, D. 1982. Thrust systems. *Bull. Am. Ass. Petrol. Geol.* **66**, 1196–1230.

Brace, W. F. & Kohlstedt, D. L. 1980. Limits on lithospheric stress imposed by laboratory experiments. *J. geophys. Res.* **85**, 6248–6252.

Chapple, W. M. 1978. Mechanics of thin-skinned fold thrust belts. *Bull. geol. Soc. Am.* **89**, 1189–1198.

Dahlen, F. A., Suppe, J. & Davis, D. M. 1984. Mechanics of fold/thrust belts and accretionary wedges: cohesive Coulomb theory. *Bull. geophys. Res.* **89**, 10,087–10,101.

Davis, D., Suppe, J. & Dahlen, F. A. 1983. Mechanics of fold and thrust belts and accretionary wedges. *J. geophys. Res.* **88**, 1153–1172.

Davis, D. & Engelder, T. 1985. The role of salt in fold/thrust belts. *Tectonophysics* **119**, 67–88.

Elliott, D. 1976. The motion of thrust sheets. *J. geophys. Res.* **81**, 949–963.

Hafner, W. 1951. Stress distributions and faulting. *Bull. geol. Soc. Am.* **62**, 373–398.

Hoshino, K., Koide, H., Inami, K., Iwamura, S. & Mitsui, S. 1972. Mechanical properties of Japanese Tertiary sedimentary rocks under high confining pressures. *Geol. Surv. Japan. Report* **244**.

Hubbert, M. K. 1951. Mechanical bases for certain familiar geologic structures. *Bull. geol. Soc. Am.* **62**, 355–372.

Hubbert, M. K. & Rubey, W. W. 1959. Role of fluid pressure in mechanics of overthrust faulting. *Bull. geol. Soc. Am.* **70**, 115–166.

Laubscher, H. P. 1977. Fold development in the Jura. *Tectonophysics* **37**, 337–362.

Mulugeta, G. 1988. Squeeze-box in a centrifuge. *Tectonophysics* **148**, 323–335.

Mulugeta, G. & Koyi, H. 1987. Three-dimensional geometry and kinematics of experimental piggyback thrusting. *Geology* **15**, 1052–1056.

Ramberg, H. 1981. *Gravity, Deformation and the Earth's Crust.* Academic Press, New York.

Zhao, W. L., Davis, D. M., Dahlen, F. A. & Suppe, J. 1986. Origin of convex accretionary wedges: evidence from Barbados. *J. geophys. Res.* **91**, 10,246–10,258.

APPENDIX

Sectioning technique

One side of a thin, rather stiff metal plate, about 0.1 mm in thickness, was coated with a thin film of paraffin wax. This metal plate was then intruded downwards along a model cross-section of interest. Heating of the metal plate to a temperature above the melting point of the paraffin or wax produced diffusion into the sand to a distance of about 0.5 cm. Upon cooling, the impregnated section stiffened to a coherent cake attached to the metal plate, which could be easily removed for detailed investigation. Since the above procedure involved removal of material sometimes during an experiment, it was necessary to fill in the space left open after removal of the cut sections in order to keep volume constant. Being uncompacted, the newly introduced material had different mechanical properties, but it was not used for monitoring progressive deformation, the next cross-section being taken at some distance from this perturbed zone during a progressive experiment. This technique has the additional advantages that model cross-sections can be stored for future use and any part of the model can be viewed under a microscope for study of grain sizes, spacings between grains and small-scale deformation structures.